Valley Hall effect in graphene-like SnX (X = Si, Ge) buckled monolayers with high charge carrier mobility and low lattice thermal conductivity

Manish Kumar Mohanta ◉,* Fathima IS ◉,* and Abir De Sarkar ◉†
Institute of Nano Science and Technology, Knowledge City, Sector 81, Mohali, Punjab 140306, India

A systematic analysis of the electronic and thermal properties of two semiconducting monolayers, SnSi and SnGe, is conducted through the lens of density functional theory. Unlike centrosymmetric graphene, these two monolayers are noncentrosymmetric and buckled in the structure; however, their band dispersion resembles that of graphene with a finite small band gap occurring at the K point of the Brillouin zone. Unlike transition metal dichalcogenide (TMDC) monolayers, the band edges in the studied semiconducting monolayers are devoid of d orbitals and contain s and p orbitals, and thus, the valley spin splitting occurring in these semiconductors is a nontrivial topological effect originating from broken inversion symmetry in the crystal structure, as observed earlier in bilayer graphene or graphene-based van der Waals heterostructures. The electronic properties are found to be tunable via external perturbations like an electric field and biaxial strain. These monolayers are highly flexible, as indicated by the small value of Young's modulus, <50 N/m. The charge carrier mobility is calculated within the Boltzmann transport equation and found to be ~ 1000 cm^2 V^{-1} s^{-1}. The phonon dynamics study indicates a very low value of lattice thermal conductivity at room temperature (i.e., $\kappa_l < 1.5$ W m^{-1} K^{-1}), which arises from the domination of Umklapp scattering, small group velocity, and low Debye temperature. Such a low value of κ_l will facilitate better thermal control than TMDCs or graphene-based devices. In this paper, we indicate that the inherent properties of SnSi and SnGe monolayers, such as valley contrasting properties, high charge carrier mobility, low lattice thermal conductivity, and mechanical flexibility, surpass that of well-known TMDCs (MoS$_2$, WS$_2$) and boron pnictides (BP, BAs, BSb), thereby motivating their synthesis.

I. INTRODUCTION

The era of two-dimensional (2D) materials commenced with the discovery of graphene [1] which shows exceptional properties compared with other bulk materials [2–4]. However, the semimetallic nature of graphene forced experimentalists to synthesize other 2D semiconductors, and some postgraphene semiconductors are transition metal dichalcogenides (TMDCs; MoS$_2$, WS$_2$) which have been studied over the past years for their exotic properties and applicability in most of the front research areas [5–7]. The semiconductor industry is presently based on utilizing the charge of carriers (electrons/holes) to store and process data. In addition to charge, electrons have spin and valley degrees of freedom, which are exploitable in spintronic and valleytronic applications. The progress in 2D materials enabled the unveiling of many physics and phenomena. Valleytronics refers to the control over the valley degree of freedom of charge carriers [8,9]. Valleys refer to the band extremum existing at the $\pm K$ point of the Brillouin zone (BZ), which can be selectively excited using an optical method [10]. The valley excitons originate from $\pm K$ valleys and are labeled by the valley index ($\pm \tau$). Since graphene is a centrosymmetric crystal, the two valleys $\pm K$ become indistinguishable, which hinders its ap-

plications in valleytronics. However, there are several ways to break the inversion symmetry such as forming van der Waals heterostructures with h-BN [11] or application of a vertical electric field in bilayer graphene [12]. Very recently, valley physics in single-layer graphene has been brought about via the breaking of triangular lattice symmetry upon laser irradiation of circularly polarized light [13]. Line defects have also been created for the purpose of inducing valley physics in graphene [14]. Therefore, it is not simple and straightforward to bring about valley physics in pristine single-layer graphene. On the other hand, the TMDCs are excellent semiconductors on account of having broken inversion symmetry and a finite direct band gap at the high-symmetry K point. The K/K' points in the first BZ of a hexagonal lattice of TMDCs are mirror images of each other under time-reversal symmetry, and a considerable magnitude of Berry curvature caused by strong spin-orbit coupling (SOC) makes an ideal platform for selective control of valley excitons. Making an imbalance of charge carriers in the inequivalent valleys results in valley polarization which is the key point to exploiting the valley degree of freedom. Magnetic proximity effect, magnetic doping, and magnetic field are some of the methods en vogue to create valley polarization [15,16]; also, they can be induced using optical pumping with circularly polarized light [10,17,18]. Some of the semiconductors proposed in addition to TMDCs include HfN$_2$ [19], Tl$_2$O [20], AgBiP$_2$Se$_6$ [21], MN$_2X_2$ [22], Janus TiXY [23] ($X \neq Y$, $X/Y = $ Cl, Br, I), CrSi$_2$N$_4$, CrSi$_2$P4 [24], NbX_2 ($X = $ S, Se) [25], heterostructures Tl/SiC

---

*These authors contributed equally to this work.
†abir@inst.ac.in; abirdesarkar@gmail.com

[26], stanene/CrI$_3$ [27], and graphene/CrI$_3$ [28]. Also, 2D magnetic materials were explored along the direction of valleytronics in search of spontaneous valley polarization [29], including VSe$_2$ [30], LaBr$_2$ [31], FeCl$_2$ [32], MnPSe$_3$ [33], VAgP$_2$Se$_6$ [34], and TiVI$_6$ [35]. Although many proposed semiconductors for valleytronics applications are listed, they are experimentally limited to TMDCs and graphene. Hence, valleytronics is still in its infancy and requires exploring materials with desired properties and functionality.

Next-generation electronics demand low power dissipation, high switching rate, and high charge carrier mobility of the semiconducting material. However, the low carrier mobility of $< 500 \, \mathrm{cm^2 \, V^{-1} \, s^{-1}}$ in TMDCs severely affects the performance of the device. Only a few valleytronics materials with an appreciable value of carrier mobility in a pristine state have been reported, e.g., H-Tl$_2$O [36] $(9.8 \times 10^3 \, \mathrm{cm^2 \, V^{-1} \, s^{-1}})$, HfN$_2$ [19] $(\sim 10^3 \, \mathrm{cm^2 \, V^{-1} \, s^{-1}})$, and BC$_6$N [37] $(8.8 \times 10^3 \, \mathrm{cm^2 \, V^{-1} \, s^{-1}})$. In addition, heterostructures have been formed to facilitate the enhancement in carrier mobility, e.g., $1T$-Sn S$_2$/Mo Te$_2$ [38] $(5038.46 \, \mathrm{cm^2 \, V^{-1} \, s^{-1}})$ and HfN$_2$/WSe$_2$ [19] $(\sim 16 \times 10^3 \, \mathrm{cm^2 \, V^{-1} \, s^{-1}})$. In addition to electronic properties, the lattice thermal conductivities of TMDCs MoS$_2$ and WS$_2$ are 33.6 W m^{-1} K^{-1} and 31.8 W m^{-1} K^{-1} [39,40], respectively, whereas that of HfN$_2$ is 0.49 W m^{-1} K^{-1} [19]. Hence, semiconducting channel materials having high charge carrier mobility and low lattice thermal conductivity are desired for next-generation devices.

In this context, based on first-principles calculations, we report two sparsely studied semiconductors, SnSi and SnGe, which exhibit stimulating electronic and thermal properties. The detailed electronic, thermal, and mechanical properties in these monolayers have been computed to elucidate the physical origin of such properties.

II. COMPUTATIONAL DETAILS

All first-principles calculations are accomplished with density functional theory (DFT) methods using the Vienna *Ab initio* Simulation Package [41,42]. The exchange-correlation interaction is described by the generalized gradient approximation (GGA) [43], having the form of the Perdew, Burke, and Ernzerhof (PBE) [44] functional with cutoff kinetic energy set to 500 eV. The BZ sampling is done by $16 \times 16 \times 1$ Γ-centered k-point mesh. Adjacent periodical structure interaction is eliminated by introducing a vacuum thickness of 15 Å in the z direction. Starting from *ab initio* electronic band structure calculation, maximally localized Wannier functions are constructed on a fine k mesh as implemented in the WANNIER90 package [45–48] and used to interpolate different physical quantities like Berry curvature and orbital magnetization in k space. The electronic band structure with SOC is calculated using QUANTUM ESPRESSO [49,50] with full relativistic optimized norm-conserving Vanderbilt pseudopotential [51–53]. The charge carrier mobility of electrons and holes is calculated within the framework of the Boltzmann transport equation (BTE). The electron-phonon coupling (EPC) matrix elements are calculated using a $15 \times 15 \times 1$ k- and q-point grid. A denser $150 \times 150 \times 1$ k- and q-point grid is used to calculate the full EPC matrix [54,55]
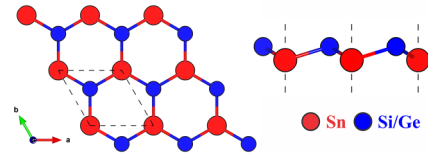

FIG. 1. The top and side views of optimized SnSi and SnGe monolayers; the unit cell is depicted by dotted lines in the left figure.

using generalized Wannier-Fourier interpolation [45,56,57] of the electron-phonon (el-ph) vertex as implemented in EPW code [58]. The second-order (harmonic) and third-order (anharmonic) interatomic force constants (IFCs) are calculated using PHONOPY [59] and PHONO3PY [60] codes. A $6 \times 6 \times 1$ supercell for second-order and $4 \times 4 \times 1$ for third-order IFCs with $9 \times 9 \times 1$ k mesh have been used in these calculations.

III. RESULTS AND DISCUSSIONS

A. Geometrical structure and stability

The optimized geometry (top and side view) of the SnSi (SnGe) monolayer is shown in Fig. 1. SnSi and SnGe monolayers have hexagonal honeycomb lattices with optimized lattice constants of 4.27 and 4.36 Å, respectively, consistent with earlier reports [61,62]. All geometrical parameters, such as buckling height, bond length, bond angle, average atomic mass, and atomic mass ratio, are tabulated in Table I. The heat of formation for SnSi (SnGe) is tabulated in Table I, and a more negative value indicates greater thermodynamic stability, whereas phonon dispersion spectra confirm their dynamical stability, as discussed later.

The heat of formation is calculated using the following relation:

$$E_h = \frac{E_{\mathrm{Sn}X} - E_{\mathrm{Sn}} - E_X}{n}, \tag{1}$$

where $E_{\mathrm{Sn}X/\mathrm{Sn}/X}$ are energies of SnX unit cells and their constituent atoms, respectively.

B. Electronic and valley contrasting properties

The electronic band structures of SnSi and SnGe are calculated using GGA-PBE and plotted in Fig. 2. Both SnSi and SnGe monolayers are direct band gap semiconductors with their valence band maxima (VBM) and conduction band minima (CBM) located at the high-symmetry K points of the hexagonal BZ with band gaps of 0.25 and 0.22 eV, respectively. The G$_0$W$_0$ band gap is 0.44 eV (0.39 eV) for the SnSi (SnGe) monolayer, as listed in Table II and plotted in Fig. S1 in the Supplemental Material (SM) [63]. The orbital projected

TABLE I. The optimized geometrical properties of SnSi, SnGe monolayers; lattice constants a_0 (Å), buckling height Δ(Å), bond lengths $b_{\mathrm{Sn}\text{-}X}$ (Å), bond angle $\Theta_{\mathrm{Sn}\text{-}X\text{-}\mathrm{Sn}}(^\circ)$, average atomic mass $\bar{M}$, the atomic mass ratio (m_X/m_{Sn}), and heat of formation (E_h).

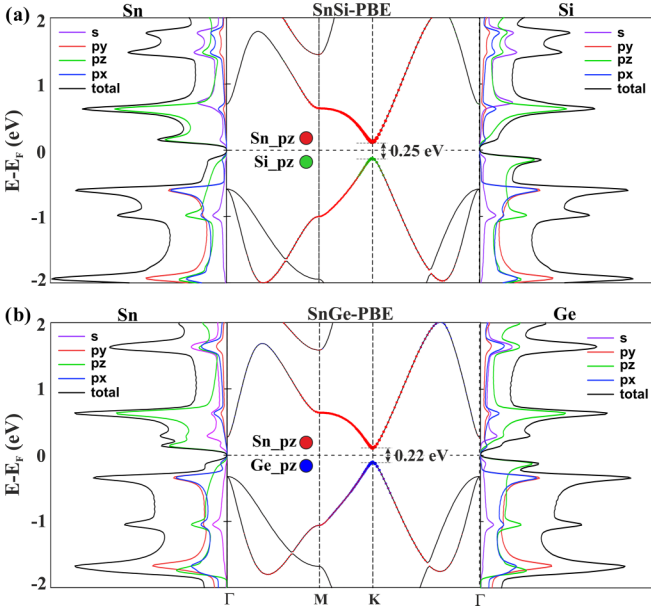| System	a_0	Δ	$b_{\mathrm{Sn}\text{-}X}$	$\Theta_{\mathrm{Sn}\text{-}X\text{-}\mathrm{Sn}}$	$\bar{M}$	m_X/m_{Sn}	E_h (eV/atom)
SnSi	4.27	0.68	2.56	113.17	73.39	0.24	−2.23
SnGe	4.36	0.77	2.63	111.83	95.68	0.61	−2.03

FIG. 2. Atomic orbital projected electronic band structure and density of states (DOS) plots of (a) SnSi and (b) SnGe monolayers. The contribution of different orbitals has been plotted with different colors in DOS, whereas only p_z orbitals of constituent atoms are projected in the band structure.

band structure indicates that the band edges are composed of individual atomic orbitals. The orbital contributions are listed in Table III. The significant contribution toward VBM and CBM is by the p_z orbitals; the VBM of the SnSi monolayer is contributed by the Si p_z orbital (72.24%), whereas that of the CBM is contributed by Sn p_z (80.77%). Similarly, in the case of the SnGe monolayer, VBM and CBM are contributed by Sn p_z (73.66%) and Ge p_z (72.54%), respectively. The same can be found in the density of states (DOS) plot. The electronic band energies are composed of the s and p orbitals, as can be analyzed from their electronic configuration:

$$Sn: [Kr]4d^{10}\,5s^2\,5p^2; \quad Si: [Ne]3s^2\,3p^2;$$

$$Ge: [Ar]3d^{10}\,4s^2\,4p^2.$$

To include the relativistic effect in electronic properties, band structures with SOC are plotted in Fig. 3. The effect of SOC can be observed in both monolayers as the band gap decreases to 0.22 eV (0.17 eV) for the SnSi (SnGe) monolayer, respectively, and the valley spin splitting (VSS) is observed in the band edges at the K valleys. The calculated VSSs at the conduction band (Δ_C) and valence band (Δ_V) edges are 8 meV (23.5 meV) and 68 meV (72 meV), respectively, for the

TABLE II. The calculated band gaps of SnX (X = Si/Ge) monolayers using different functionals.

Monolayers	Band gap (eV)		
	PBE	PBE-SOC	G_0W_0
SnSi	0.25	0.22	0.44
SnGe	0.22	0.17	0.39

SnSi (SnGe) monolayer. The Δ_C of these monolayers is comparable with VSSs in MoSSe ($\Delta_C = 13.7$ meV) and WSSe ($\Delta_C = 26.8$ meV), whereas Δ_V of the SnSi (Ge) monolayer is of the order of the VSSs in the CrS_2 (68.5 meV) and $CrSe_2$ (90.6 meV) monolayers [64–66]. Considering the orbital composition of the band edges, both SnSi and SnGe are analogous to bilayer graphene or graphene/h-BN systems, as these materials have minimal spin-orbit interaction but exhibit valley splitting by virtue of broken inversion symmetry [67–70]. For a better representation, the Berry curvatures along with orbital magnetization of both monolayers have been calculated from Wannier interpolation [48,71,72] and shown in Fig. 3. Both semiconductors have finite Berry curvatures and orbital magnetization. Similarly, a previous study of valley splitting in bilayer graphene indicates that the valley degrees of freedom have a nontrivial topology that gives rise to a Berry curvature and a pseudo-orbital magnetic moment [73].

The equation of motion of Bloch electrons under periodic potential and the magnetic field is given by [74]

$$\hbar v_n(k) = \frac{\partial \varepsilon_n(k)}{\partial k} - eE\,\Omega_n(k). \tag{2}$$

The anomalous velocity obtained is proportional to the Berry curvature $\Omega_n(k)$, represented by the second term in the above equation. The Berry curvature acts as an effective magnetic field to the Bloch electron. The Berry curvatures as contour maps over the entire BZ $\Omega_n(k)$ for both monolayers are calculated and plotted in Fig. 4, using the Kubo formula given by [75–77]

$$\Omega_n(k) = -\sum_n \sum_{m \neq n} f_n \frac{2\mathrm{Im}\langle \psi_{nk}|\hat{v}_x|\psi_{mk}\rangle\langle\psi_{mk}|\hat{v}_y|\psi_{nk}\rangle}{(E_{nk} - E_{mk})^2}. \tag{3}$$

Here, f_n is the Fermi-Dirac distribution function, ψ_{nk} is the Bloch wave function with energy eigenvalue E_n, and $\hat{v}_{x,y}$ corresponds to velocity operators along x and y directions. An optical selection rule arises in the K/K' valleys of hexagonal honeycomb lattices lacking inversion symmetry. The relationship between Berry curvature and optical circular dichroism is given by [78]

$$\eta(k) = -\frac{\Omega_n(k)}{\mu_B^*(k)}\frac{e}{2\hbar}\Delta(k), \tag{4}$$

where $\mu_B^*(k) = e\hbar/2m^*$, and $\Delta(k) = [\varepsilon_c(k) - \varepsilon_v(k)]$ is the direct transition energy (band gap at k). The circular dichroism is evaluated with the DFT calculation and plotted in Fig. 4. Full selectivity occurs for energetic minima at the K and K' points, while $\eta(k) = -\tau_Z$. The right-handed circularly polarized light (σ^+) can be coupled to the interband transition at the K valley and the left-handed circularly polarized light (σ^-) for exciting the charge carriers from the K' valley, as shown in Fig. 5. Under optical excitation, the Bloch carriers at K and K' will drift in opposite directions because of anomalous velocity under the influence of an in-plane electric field, as governed by Eq. (2). In addition to selective excitation of carriers with circularly polarized light, spin-dependent excitation is also feasible with different excitation frequencies, as denoted by ω_u (blue) and ω_d (red). The coupling of valley and spin is highly desirable for the practical realization of valleytronic devices, which can be achieved using different

TABLE III. Orbital contribution to the VBM and CBM of SnSi and SnGe monolayers.

		VBM				CBM				VSS at conduction and valence band edges	
		s	p_y	p_x	p_z	s	p_y	p_x	p_z	Δ_C (meV)	Δ_V (meV)
SnSi	Sn	0	7.76	7.76	0	8.46	0	0	80.77	8	58
	Si	7.4	0	0	72.24	0	5.26	5.26	0		
SnGe	Sn	0	8.7	8.7	0	8.5	0	0	73.66	23.5	72
	Ge	7	0	0	72.54	0	8.13	8.13	0		

excitation frequencies. For instance, in a hole-doped system, as a result of valley-contrasting Berry curvatures, the holes from the K valley (green) and K' valley (blue color) will be accumulated at the edges as their motion will be perpendicular to the in-plane electric field realizing spin and valley Hall effect [79], as shown in Fig. 5. Similarly, under linear polarized light radiation with a frequency ω_u, a spin-up electron and a spin-down hole from the K valley and a spin-down electron and a spin-up hole from the K' valley are generated, and in the presence of the electric field, their motional dynamics is pictorially presented in Fig. 5(c).

C. Electronic properties under external perturbation

Electronic properties can be manipulated using external stimuli like strain and electric field experimentally and theoretically [80–85]. In this section, a thorough analysis of the transformation of band structure under both strain and electric fields is conducted. The variation of the band gap of the SnSi monolayer under biaxial strain is plotted in Fig. 6. Here, strain is defined as $\frac{a-a_0}{a_0}$, where a_0 is the unperturbed lattice constant. The band gap changes from direct to indirect and from semiconducting to a metallic state under biaxial strain are observed here. The band structures of selected strains are plotted for visualization of different transitions. In the interest of the experimentalists, different kinds of strain within the

experimentally feasible range, i.e., ±3%, have been applied to the SnSi monolayer, and Fig. S2 in the SM [63] depicts how the band gap evolves with different types of strain. The band gaps are found to be direct in nature in all cases except under tensile strain applied along the b direction. It is clear that, whereas the band gap changes linearly with biaxial strain from −3 to +3%, band gap variation with the application of uniaxial strain along the a and b directions is complementary to one another. Further, uniaxial compressive strain applied along the b direction is found to be quite effective for opening the band gap, which remains direct in SnSi monolayer. The strain-induced transition from direct to indirect band gap, say, under biaxial strain >2%, as shown in Fig. 6, will manifest experimentally through a drastic reduction in photoluminescence [86], while the same from semiconducting to a metallic state, occurring at higher strain percentage, can be exploited in electronics. A small 4% biaxial tensile strain results in a metallic state, as plotted in Fig. 6, which indicates their sensitivity to external strain. Similarly, the results under strain for SnGe are provided in Fig. S3 in the SM [63].

Next, a perpendicular electric field is applied, as schematically shown in Fig. 7, along with the variation in the band gap of SnSi. The band gap increases under a positive electric field, whereas it closes under a small magnitude of negative/reverse electric field, and the shifting of CBM and VBM under an electric field is marked and shown in Fig. 7(d). The band gap
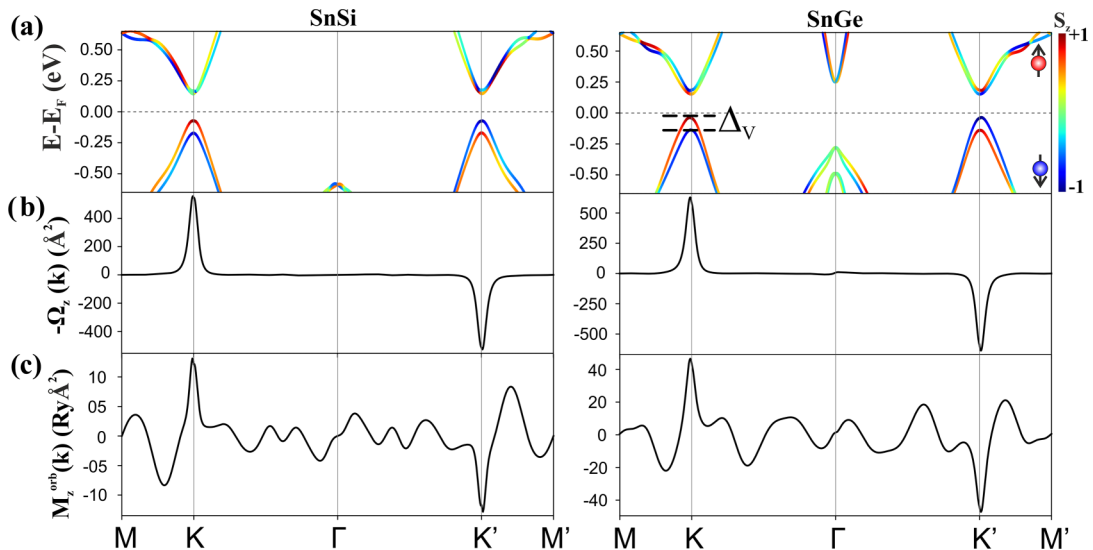

FIG. 3. (a) Calculated band structure including relativistic effect; Δ_v represents valley spin splitting occurs at the valence band maximum (VBM) at the K point, (b) calculated Berry curvature (Ω_z), and (c) orbital magnetization (M_z^{orb}) of SnSi and SnGe monolayers.
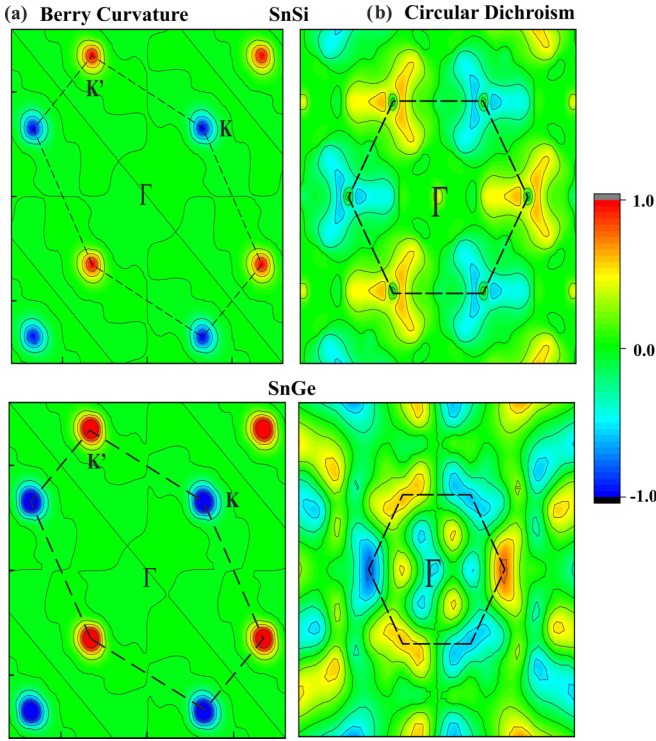
FIG. 4. (a) Calculated Berry curvature and (b) circular dichroism in the two-dimensional (2D) Brillouin zone for SnSi and SnGe monolayers.

FIG. 6. (a) The band gap tunability of the SnSi monolayer with the application of biaxial strain (b) and (c) band structures under different strains as indicated in the figure; blue and red dots represent valence band maximum (VBM) and conduction band minimum (CBM), respectively.

evolution of SnGe under a vertical electric field is plotted in Fig. S4 in the SM [63]. The important point to be noted is that band closure is achievable for a very small negative electric field of ~ -0.25 V/Å in both SnSi and SnGe mono-

layers, which makes it promising for low-power switching applications.

From the electric-field-dependent electronic properties study, it can be concluded that a positive electric field will be more interesting than strain or a negative electric field as the band gap opens. Hence, small electric field within 0.2 V/Å is chosen where both monolayers remain direct band gap at the K point, and VSSs at both CBM (Δ_C) and VBM (Δ_V) are plotted for SnSi and SnGe monolayers in Fig. 8. Although there is a slight variation in VSS under an electric field, VSS can be considered robust against a small positive electric field.

D. Mechanical constants and charge carrier mobility

The mechanical stability of these materials has been confirmed via Born-Huang stability criteria:

$$C_{11} > |C_{12}|, \quad C_{22} > 0, \quad C_{66} > 0, \quad C_{11}C_{22} - C_{12}^2 > 0. \tag{5}$$

The elastic stiffness coefficients C_{11}, C_{12}, and C_{22} which are the most significant for any 2D material were calculated for SnSi and SnGe monolayers using the strain-energy relationship as incorporated in VASPKIT [87] and tabulated in Table IV. Further other mechanical parameters can be derived from obtained C_{ij} as follows:

$$\text{Young's modulus } Y = \frac{C_{11}^2 - C_{12}^2}{C_{11}}, \tag{6}$$

$$\text{Shear modulus} = C_{66}, \tag{7}$$

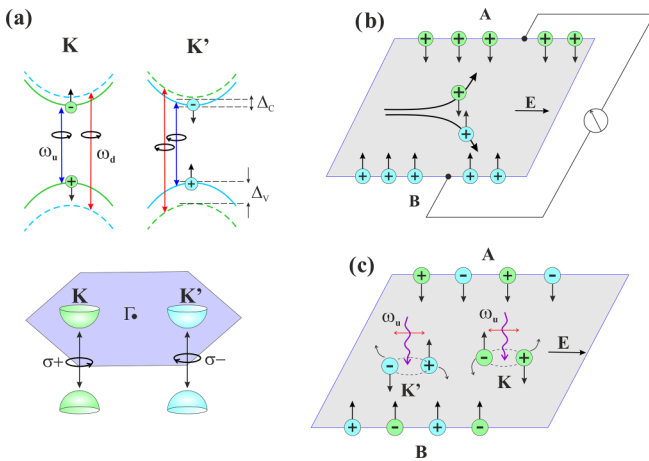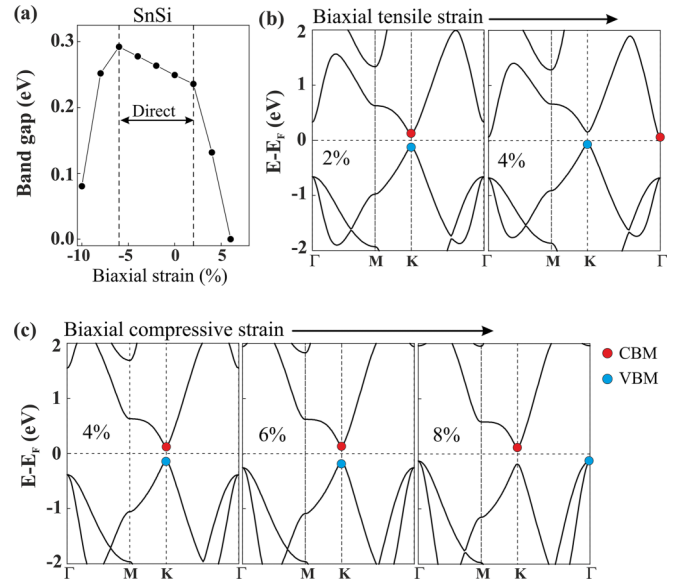$$\text{Poisson's ratio } v = \frac{C_{12}}{C_{11}}. \tag{8}$$

FIG. 5. (a) Schematic diagram of valley spin splitting in the valence and conduction band edges at the K/K' point; the green and cyan hemispheres represent charge carriers in the K and K' valleys, respectively; symbols $+$ and $-$ represent holes and electrons, respectively; blue and red arrows show the optical transition frequencies ω_u and ω_d, respectively; $\sigma+/\sigma-$ represent right-/left-handed circularly polarized light, spin, and valley Hall effect; (b) under hole doping and (c) under linearly polarized optical field with a frequency ω_u.
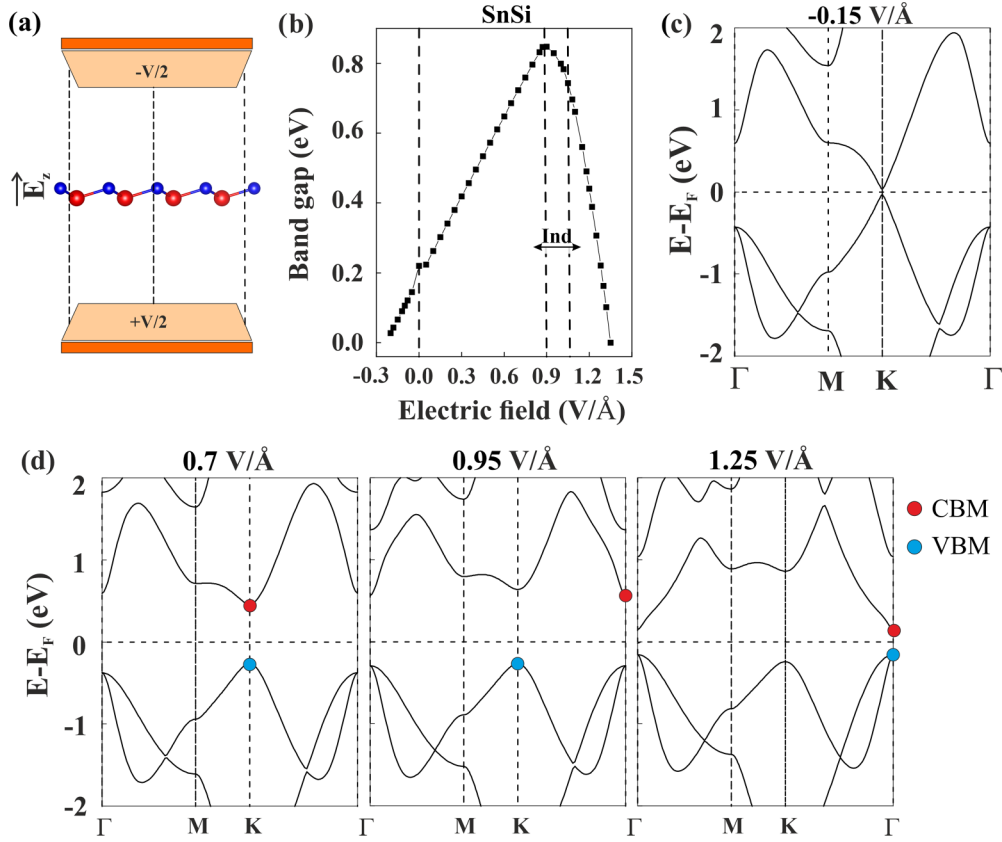
FIG. 7. (a) Schematic of the application of vertical electric field, (b) band gap of the SnSi monolayer under vertical electric field, (c) and (d) band structure under different field directions; red and blue circles represent conduction band minimum (CBM) and valence band maximum (VBM), respectively.

The low value of Young's modulus for both monolayers represents their flexibility, which is comparable with CdTe (25.63N/m) [88], ZnTe (31.73 N/m) [88], and MgTe (29.13 N/m) [89] and smaller than the other monolayers such as h-BN (271 N/m) [90], MoS_2 (118–141 N/m) [91,92], BP (152.41 N/m), BAs (135.68 N/m), and BSb (107.19 N/m) [93].

The charge carrier mobility, which plays a key role in determining the performance of a semiconductor in electronic devices, is dependent on the EPC strength. In earlier studies,

the deformation potential (DP) theory proposed by Bardeen and Shockley [94] was extensively used to calculate charge carrier mobility in 2D materials [95,96] on account of its relative simplicity. This formalism requires only a few material properties such as effective mass, elastic stiffness constant, and carrier DP (i.e., slope of the shift in the band edges under infinitesimal uniaxial strain) as inputs [97]. Moreover, it only considers scattering from longitudinal-acoustic phonons, while optical phonon scatterings are excluded. The latter have been shown to be a crucial factor in carrier scatterings at room temperatures, such as in 2D MoS_2 [98]. Therefore, the BTE method beyond effective mass approximation has been employed here to calculate the charge carrier mobility.

The phonon-limited charge carrier mobility is calculated as [99,100]

$$\mu_{\alpha\beta} = -\frac{1}{\Omega n_c} \sum_{n \in CB} \int \frac{d^3k}{\Omega_{BZ}} v_{nk,\alpha} \partial_{E_\beta} f_{nk}, \qquad (9)$$
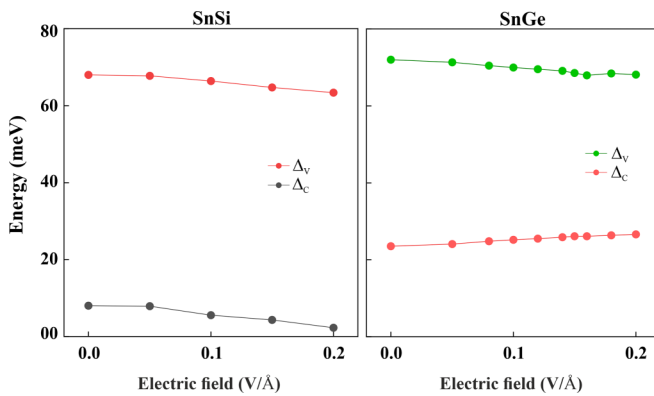

FIG. 8. The variation of valley spin splitting (VSS) at the valence band maximum (VBM; Δ_V) and conduction band minimum (CBM; Δ_C) under the application of small vertical electric field.

TABLE IV. Elastic stiffness constants C (N/m), Young's modulus Y (N/m), shear moduli G_{xy} (N/m), and Poisson ratio (v) calculated for SnX (X = Si, Ge) monolayers.

System	C_{11}	C_{22}	C_{12}	Y	G_{xy}	v	Stability
SnSi	53.35	53.35	12.75	50.3	20.3	0.24	Stable
SnGe	44.41	44.41	10.47	41.94	16.96	0.24	Stable

TABLE V. Calculated charge carrier mobility of SnX (within BTE) and other valley and nonvalley semiconductors (using DP theory [94,102–104]).

2D semiconductors	Charge carrier mobility (cm^2 V^{-1} s^{-1})	
	Electron	Hole
SnSi (This paper)	1176.6 (xx)/1190.7 (yy)	704 (xx)/800.6 (yy)
SnGe (This paper)	855.3 (xx)/831.3 (yy)	810.9 (xx)/810.5 (yy)
h-BP [105]	∼50 × 10^3	∼10 × 10^3
h-BAs [105]	∼70 × 10^3	∼30 × 10^3
HfN$_2$ [19]	1.18 × 10^3	5.93 × 10^3
MoS$_2$ [106,107]	0.072 × 10^3	0.060 × 10^3
WS$_2$ [106,107]	0.12 × 10^3	0.21 × 10^3

where Ω is the volume of the unit cell, n_c is the charge concentration, Ω_{BZ} is the volume of the BZ, $\partial_{E_\beta} f_{nk}$ is the derivative of the occupation function f_{nk} with respect to the electric field E, and $v_{nk,\alpha} = \hbar^{-1} \frac{\partial \epsilon_{nk}}{\partial k_\alpha}$ is the band velocity for the Kohn-Sham state ϵ_{nk}. The scattering rate (τ_{nk}^{-1}) defined as the inverse of el-ph relaxation time can be directly calculated from the imaginary part of the el-ph self-energy ImΣ_{nk} using $\tau_{nk}^{-1} = \frac{2}{\hbar} \text{Im} \Sigma_{nk}$ which is expressed as

$$\tau_{nk}^{-1} = \frac{2\pi}{\hbar} \sum_{qv,m} |g_{mn,v}(k, q)|^2$$

$$\times [(n_{q,v} + f_{k+q,m})\delta(\epsilon_{k+q,m} - \epsilon_{k,n} - \hbar\omega_{q,v})$$

$$+ (1 + n_{q,v} - f_{k+q,m})\delta(\epsilon_{k+q,m} - \epsilon_{k,n} + \hbar\omega_{q,v})], \quad (10)$$

where $\hbar\omega_{q,v}$ is the frequency, and $n_{q,v}$ is the occupation (using Bose-Einstein statistics) of the phonon mode v at wave vector q. The el-ph matrix elements $g_{mn,v}(k, q)$ are the amplitude for scattering from an initial state n, **k** to a final state m, **k** + q. The two Dirac delta functions indicate the energy conservation conditions for el-ph scattering events, with the former corresponding to a phonon absorption process and the latter to a phonon emission process. Treating the static electric field as a small perturbation, $\partial_{E_\beta} f_{nk}$ can be solved iteratively, and the electron mobility is obtainable from an iterative solution of the linearized BTE [100,101]. The charge carrier mobilities of SnSi and SnGe monolayers are tabulated in Table V.

E. Phonon dynamics

The lattice thermal conductivity (κ_l) of a phonon in the i direction is obtained by solving the BTE under relaxation time approximation and using the Fourier law given by [108]

$$\kappa_{l,i} = \sum_\lambda \sum_q c_{ph} v_{g,i}^2(q, \lambda)\tau(q, \lambda). \quad (11)$$

The summation is over all phonon modes with wave vector q and dispersion branch λ, c_{ph} is specific heat capacity, $v_{g,i}$ is the i component of the group velocity, and $\tau(q, \lambda)$ is the relaxation time of the phonon mode with wave vector q.

The specific heat capacity is calculated using harmonic approximation, whereas for the calculation of phonon lifetime, anharmonic contributions must be included where phonon-phonon interaction is considered. In the harmonic
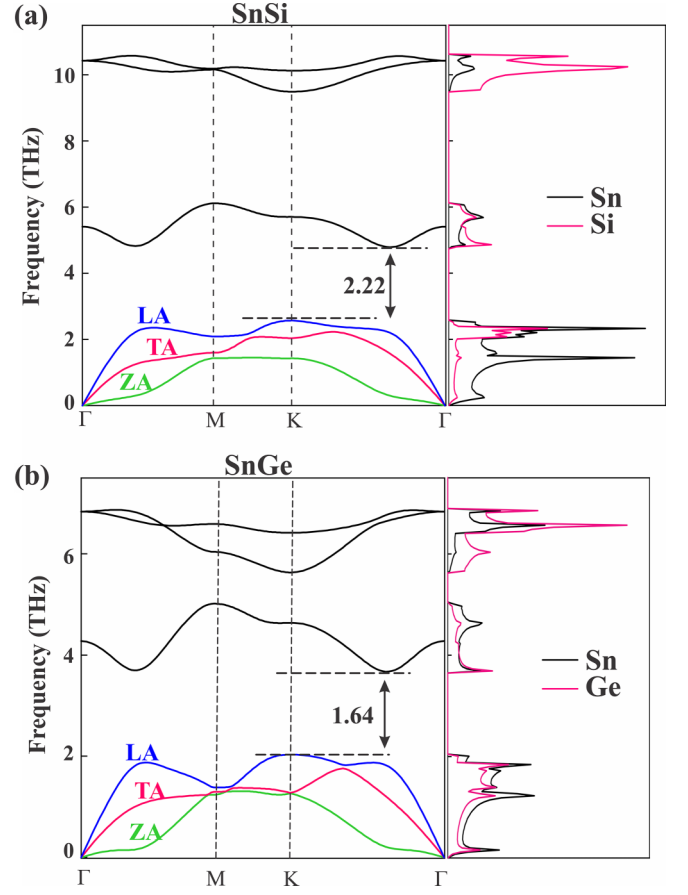

FIG. 9. Phonon dispersions and the partial atomic phonon density of SnSi and SnGe monolayer states. Green, pink, and violet represent the three acoustic phonons, and black represents the optical phonons.

approximation, the phonon frequencies have been calculated using density functional perturbation theory. The phonon dispersion, along with the phonon DOS (PhDOS) for the SnSi and SnGe monolayers, is plotted in Fig. 9. The zoomed image of acoustic phonon spectra near the Γ point indicates the q^2 feature, as plotted in Fig. S5 in the SM [63]. There are two atoms in the unit cell, which results in six phonon branches: three acoustic phonons (LA, TA, and ZA) and three optical phonons as distinguished by different colors. From the Ph-DOS, the acoustic phonon modes are contributed from both atomic vibrations.

The group velocity of each mode of vibration is determined from the phonon dispersion directly using the relation [109] $v_{iq} = \frac{\partial \omega_{i,q}}{\partial q}$ and plotted in Fig. 10. The maximum group velocity of SnSi and SnGe are 5 and 4.2 km/s, respectively. The group velocities obtained for these monolayers are comparable with that of germanene (1.39 km/s) [110], phosphorene (7.7 km/s) [111], silicene (5.4–8.8 km/s) [112], and stanene (1.3–3.6 km/s) [113]. The numerical solution of phonon relaxation can be obtained by the phonon line width using the below relation [60]:

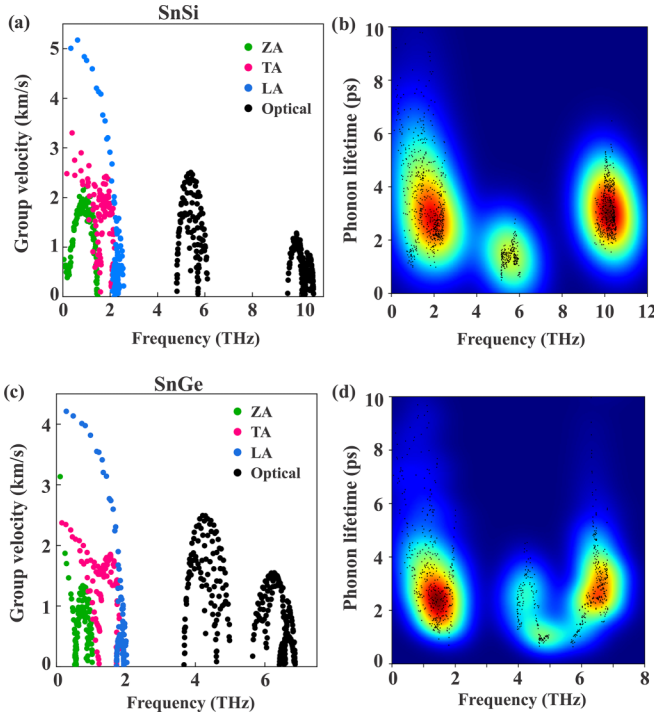$$\tau_i = \frac{1}{2\Gamma_i(\omega_i)}, \quad (12)$$

FIG. 10. Calculated phonon group velocity and lifetime for (a) and (b) SnSi monolayer and (c) and (d) SnGe monolayer.
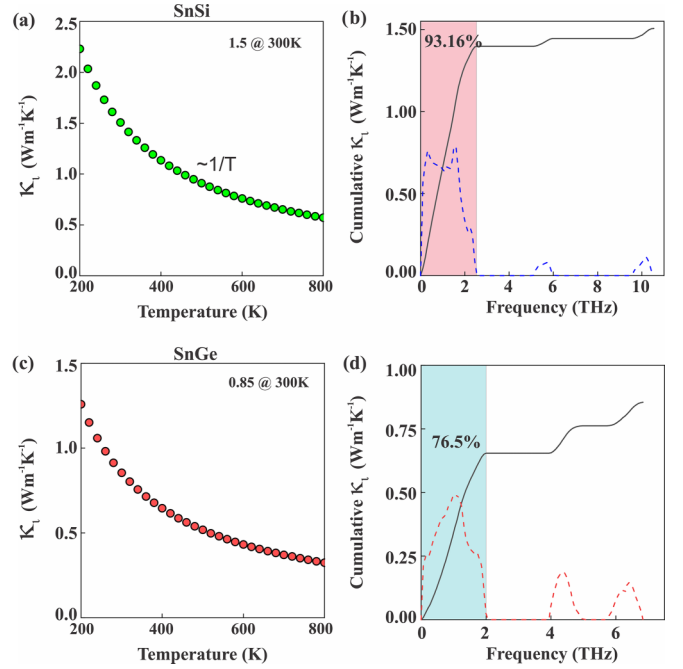

FIG. 11. Calculated lattice thermal conductivity at different temperatures and cumulative lattice thermal conductivities of (a) and (b) SnSi monolayer and (c) and (d) SnGe monolayer.

where the $\Gamma_i(\omega_i)$ is analogous to the Fermi golden rule and completely incorporates scatterings from all phonon modes. The phonon lifetime obtained for the SnSi (SnGe) monolayer is plotted as shown in Fig. 10. The very short lifetime of phonons indicates a high phonon-phonon scattering rate, as they are inversely proportional to each other. Such a short phonon lifetime is comparable with that of ZnX (X = S, Se, Te) [88].

Further, the Debye temperature calculation can be calculated from the phonon dispersion given by [110,114]

$$\frac{1}{\theta_D^3} = \frac{1}{3}\left(\frac{1}{\theta_{ZA}^3} + \frac{1}{\theta_{TA}^3} + \frac{1}{\theta_{LA}^3}\right), \quad (13)$$

where $\theta_A = h v_m/k_B$, where $\hbar$ is the Planck constant, v_m represents the maximum frequency of the mode, and k_B is the Boltzmann constant. Table VI contains the Debye temperature of the SnGe monolayer. The Debye temperature obtained for SnSi (87.63 K) and SnGe (65.15 K) monolayers are of the

TABLE VI. Calculated Debye temperature (Θ_D; in K) of SnSi and SnGe monolayers from phonon frequency of three acoustic branches; v_m, the maximum frequency corresponding to normal mode vibration.

System	Phonon modes	v_m (THz)	Θ_A	Θ_D (K)
SnSi	ZA	1.43	68.64	87.63
	TA	2.22	106.55	
	LA	2.56	122.87	
SnGe	ZA	1.03	49.44	65.15
	TA	1.83	87.83	
	LA	2.02	96.95	

order of that of stanene (72.5 K) and very low compared with graphene (2300 K) and MoS$_2$ (262.3 K). In accordance with the Slack theory [115], a low Debye temperature implies low thermal conductivity because a low Debye temperature corresponds to a low phonon velocity and low acoustic-phonon frequencies, which leads to an increase in phonon scattering rate (decrease in a phonon lifetime) as a result of increased phonon population. Also, it can be predicted that the bond strength of the material in terms of the low value of Young's modulus in the SnSi (SnGe) monolayer also leads to low group velocity and hence the ultralow thermal conductivity.

The temperature-dependent lattice thermal conductivities of SnSi and SnGe monolayers are plotted in Fig. 11. The lattice thermal conductivity value of the SnSi (SnGe) monolayer at 300 K is found to be 1.5 W/mK (0.85 W/mK), which is of the order of reported 2D materials with ultralow thermal conductivity such as SnSe$_2$ [116] (1.74 W/mK), SbAs [117] (1.60 W/m K), SnSe [118] (2.63 W/mK), and dumbbell silicene [119] (2.86 W/mK). For a systematic comparison, the lattice thermal conductivities of other well-known valleytronic semiconductors are provided in Table VII. It can also be seen that the Umklapp scattering is dominant in these systems, as they follow a $1/T$ relation, as marked in Fig. 11. The shaded region of this plot is the cumulative lattice thermal conductivity which highlights the contribution of acoustic phonon modes toward heat transportation. It is found that acoustic phonons dominate in the case of SnSi (93.16%), whereas optical phonons (23%) contribute to the SnGe monolayer. Considering the three-phonon scattering mechanism ($a + a \leftrightarrow a; a + a \leftrightarrow 0$), the acoustic and optical gap decreases significantly in case of SnGe, as marked in Fig. 9, and hence, the contribution of optical mode increases [88,89,110].

TABLE VII. Lattice thermal conductivity of well-known valleytronics material for comparison.

2D semiconductors	Lattice thermal conductivity (W m^{-1} K^{-1})
SnGe (this paper)	0.85
SnSi (this paper)	1.5
HfN$_2$ [19]	0.49
MoS$_2$ [39,40]	33.6
MoSe$_2$ [39]	17.8
MoTe$_2$ [40]	16.3
WS$_2$ [39]	31.8
WSe$_2$ [40]	18.2
h-BP [93]	51.3
h-BAs [93]	20.7

IV. CONCLUSIONS

In this paper, we introduce two buckled semiconducting monolayers, SnX (X = Si, Ge), having properties similar to and yet different from that of graphene. Both monolayers are found to be direct band gaps, whereas the band dispersion resembles that of graphene. These two semiconducting monolayers exhibit VSSs at the K/K' point, which originates from their crystal structure and is found to be robust against a small electric field. Additionally, small biaxial strain and a negative electric field can be applied to close the band gap in these monolayers, which will be useful in low-power switching applications, whereas a positive electric field can be used to open the band gap. Low lattice thermal conductivity in the semiconducting monolayers, as noted in this paper, originates from the dominance of Umklapp scattering, low group velocity, and low Debye temperature. Moreover, these two semiconductors exhibit rich spin-valley physics, high flexibility, high charge carrier mobility, and low lattice thermal conductivity, which shows their immense potential in the field of valleytronics, nanoelectronics, and flexoelectronic devices and thermoelectricity.

[1] K. S. Novoselov, A. K. Geim, S. V. Morozov, D. Jiang, Y. Zhang, S. V. Dubonos, I. V. Grigorieva, and A. A. Firsov, Electric field effect in atomically thin carbon films, Science **306**, 666 (2004).

[2] L. A. Falkovsky and S. S. Pershoguba, Optical far-infrared properties of a graphene monolayer and multilayer, Phys. Rev. B **76**, 153410 (2007).

[3] H.-J. Lee, E. Kim, W.-J. Lee, and J. Jung, RF transmission properties of graphene monolayers with width variation, Phys. Status Solidi RRL **6**, 19 (2012).

[4] D. S. L. Abergel, V. Apalkov, J. Berashevich, K. Ziegler, and T. Chakraborty, Properties of graphene: A theoretical perspective, Adv. Phys. **59**, 261 (2010).

[5] O. Omar, Monolayer MoS$_2$/n-Si heterostructure Schottky solar cell, J. Renew. Mater. **10**, 1979 (2022).

[6] X. Yang and B. Li, Monolayer MoS$_2$ for nanoscale photonics, Nanophotonics **9**, 1557 (2020).

[7] L. Liu, K. Ye, Z. Yu, Z. Jia, J. Xiang, A. Nie, F. Wen, C. Mu, B. Wang, Y. Li *et al.*, Photodetection application of one-step synthesized wafer-scale monolayer MoS$_2$ by chemical vapor deposition, 2D Mater. **7**, 025020 (2020).

[8] J. R. Schaibley, H. Yu, G. Clark, P. Rivera, J. S. Ross, K. L. Seyler, W. Yao, and X. Xu, Valleytronics in 2D materials, Nat. Rev. Mater. **1**, 16055 (2016).

[9] D. Xiao, W. Yao, and Q. Niu, Valley-Contrasting Physics in Graphene: Magnetic Moment and Topological Transport, Phys. Rev. Lett. **99**, 236809 (2007).

[10] K. F. Mak, K. He, J. Shan, and T. F. Heinz, Control of valley polarization in monolayer MoS$_2$ by optical helicity, Nat. Nanotech. **7**, 494 (2012).

[11] R. V. Gorbachev, J. C. W. Song, G. L. Yu, A. V. Kretinin, F. Withers, Y. Cao, A. Mishchenko, I. V. Grigorieva, K. S. Novoselov, L. S. Levitov *et al.*, Detecting topological currents in graphene superlattices, Science **346**, 448 (2014).

[12] M. Sui, G. Chen, L. Ma, W.-Y. Shan, D. Tian, K. Watanabe, T. Taniguchi, X. Jin, W. Yao, D. Xiao *et al.*, Gate-tunable topological valley transport in bilayer graphene, Nature Phys. **11**, 1027 (2015).

[13] M. S. Mrudul, Á. Jiménez-Galán, M. Ivanov, and G. Dixit, Light-induced valleytronics in pristine graphene, Optica **8**, 422 (2021).

[14] D. Gunlycke and C. T. White, Graphene Valley Filter Using a Line Defect, Phys. Rev. Lett. **106**, 136806 (2011).

[15] R. Peng, Y. Ma, S. Zhang, B. Huang, and Y. Dai, Valley polarization in Janus single-layer MoSSe via magnetic doping, J. Phys. Chem. Lett. **9**, 3612 (2018).

[16] L. Xu, M. Yang, L. Shen, J. Zhou, T. Zhu, and Y. P. Feng, Large valley splitting in monolayer WS$_2$ by proximity coupling to an insulating antiferromagnetic substrate, Phys. Rev. B **97**, 041405(R) (2018).

[17] H. Zeng, J. Dai, W. Yao, D. Xiao, and X. Cui, Valley polarization in MoS$_2$ monolayers by optical pumping, Nat. Nanotechnol. **7**, 490 (2012).

[18] A. M. Jones, H. Yu, N. J. Ghimire, S. Wu, G. Aivazian, J. S. Ross, B. Zhao, J. Yan, D. G. Mandrus, D. Xiao *et al.*, Optical generation of excitonic valley coherence in monolayer WSe$_2$, Nature Nanotech **8**, 634 (2013).

[19] M. K. Mohanta and A. De Sarkar, Coupled spin and valley polarization in monolayer HfN$_2$ and valley-contrasting physics at the HfN$_2$/WSe$_2$ interface, Phys. Rev. B **102**, 125414 (2020).

[20] Y. Ma, L. Kou, A. Du, B. Huang, Y. Dai, and T. Heine, Conduction-band valley spin splitting in single-layer H-Tl$_2$O, Phys. Rev. B **97**, 035444 (2018).

[21] Q. Pei, B. Zhou, W. Mi, and Y. Cheng, Triferroic material and electrical control of valley degree of freedom, ACS Appl. Mater. Interfaces **11**, 12675 (2019).

[22] K. Dou, Y. Ma, R. Peng, W. Du, B. Huang, and Y. Dai, Promising valleytronic materials with strong spin-valley coupling in two-dimensional MN_2X_2 (M = Mo, W; X = F, H), Appl. Phys. Lett. **117**, 172405 (2020).

[23] Y. Wang, W. Wei, H. Wang, N. Mao, F. Li, B. Huang, and Y. Dai, Janus TiXY monolayers with tunable berry curvature, J. Phys. Chem. Lett. **10**, 7426 (2019).

[24] Y. Liu, T. Zhang, K. Dou, W. Du, R. Peng, Y. Dai, B. Huang, and Y. Ma, Valley-contrasting physics in single-layer $CrSi_2N_4$ and $CrSi_2P_4$, J. Phys. Chem. Lett. **12**, 8341 (2021).

[25] Y. Zang, Y. Ma, R. Peng, H. Wang, B. Huang, and Y. Dai, Large valley-polarized state in single-layer NbX_2 (X = S, Se): Theoretical prediction, Nano Res. **14**, 834 (2021).

[26] Z. Xu, Q. Zhang, Q. Shen, Y. Cheng, U. Schwingenschlögl, and W. Huang, First-principles prediction of Tl/SiC for valleytronics, J. Mater. Chem. C **5**, 10427 (2017).

[27] B. Zhai, J. Du, C. Shen, T. Wang, Y. Peng, Q. Zhang, and C. Xia, Spin-dependent Dirac electrons and valley polarization in the ferromagnetic stanene/CrI_3 van der Waals heterostructure, Phys. Rev. B **100**, 195307 (2019).

[28] M. U. Farooq and J. Hong, Switchable valley splitting by external electric field effect in graphene/CrI_3 heterostructures, npj 2D Mater. Appl. **3**, 3 (2019).

[29] T. Zhang, X. Xu, B. Huang, Y. Dai, and Y. Ma, 2D spontaneous valley polarization from inversion symmetric single-layer lattices, npj Comput. Mater. **8**, 64 (2022).

[30] J. Liu, W.-J. Hou, C. Cheng, H.-X. Fu, J.-T. Sun, and S. Meng, Intrinsic valley polarization of magnetic VSe_2 monolayers, J. Phys.: Condens. Matter **29**, 255501 (2017).

[31] P. Zhao, Y. Ma, C. Lei, H. Wang, B. Huang, and Y. Dai, Single-layer $LaBr_2$: Two-dimensional valleytronic semiconductor with spontaneous spin and valley polarizations, Appl. Phys. Lett. **115**, 261605 (2019).

[32] P. Zhao, Y. Dai, H. Wang, B. Huang, and Y. Ma, Intrinsic valley polarization and anomalous valley Hall effect in single-layer 2H-$FeCl_2$, ChemPhysMater **1**, 56 (2021).

[33] X. Li, T. Cao, Q. Niu, J. Shi, and J. Feng, Coupling the valley degree of freedom to antiferromagnetic order, Proc. Natl. Acad. Sci. USA **110**, 3738 (2013).

[34] Z. Song, X. Sun, J. Zheng, F. Pan, Y. Hou, M.-H. Yung, J. Yang, and J. Lu, Spontaneous valley splitting and valley pseudospin field effect transistors of monolayer VAgP_2Se$_6$, Nanoscale **10**, 13986 (2018).

[35] W. Du, Y. Ma, R. Peng, H. Wang, B. Huang, and Y. Dai, Prediction of single-layer $TiVI_6$ as a promising two-dimensional valleytronic semiconductor with spontaneous valley polarization, J. Mater. Chem. C **8**, 13220 (2020).

[36] Y. Ma, A. Kuc, and T. Heine, Single-layer Tl_2O: A metal-shrouded 2D semiconductor with high electronic mobility, J. Am. Chem. Soc. **139**, 11694 (2017).

[37] L.-B. Shi, M. Yang, S. Cao, Q. You, Y.-J. Zhang, M. Qi, K.-C. Zhang, and P. Qian, Prediction of high carrier mobility for a novel two-dimensional semiconductor of BC_6N: First principles calculations, J. Mater. Chem. C **8**, 5882 (2020).

[38] S. Teng, J. Li, X. Mao, F. He, Z. Liu, J. Wang, and Y. Wang, Large Rashba splitting, carrier mobility, and valley polar-

[39] ization in a $1T$-SnS_2/$MoTe_2$ heterostructure, Phys. Chem. Chem. Phys. **23**, 16242 (2021).

[39] B. Peng, H. Zhang, H. Shao, Y. Xu, X. Zhang, and H. Zhu, Thermal conductivity of monolayer MoS_2, $MoSe_2$, and WS_2: Interplay of mass effect, interatomic bonding and anharmonicity, RSC Adv. **6**, 5767 (2016).

[40] M. Zulfiqar, Y. Zhao, G. Li, Z. Li, and J. Ni, Intrinsic thermal conductivities of monolayer transition metal dichalcogenides MX_2 (M = Mo, W; X = S, Se, Te), Sci. Rep. **9**, 4571 (2019).

[41] G. Kresse and J. Furthmüller, Efficient iterative schemes for *ab initio* total-energy calculations using a plane-wave basis set, Phys. Rev. B **54**, 11169 (1996).

[42] G. Kresse and J. Furthmüller, Efficiency of *ab-initio* total energy calculations for metals and semiconductors using a plane-wave basis set, Comput. Mater. Sci. **6**, 15 (1996).

[43] J. P. Perdew, K. Burke, and M. Ernzerhof, Generalized Gradient Approximation Made Simple, Phys. Rev. Lett. **77**, 3865 (1996).

[44] P. E. Blöchl, Projector augmented-wave method, Phys. Rev. B **50**, 17953 (1994).

[45] A. A. Mostofi, J. R. Yates, Y.-S. Lee, I. Souza, D. Vanderbilt, and N. Marzari, WANNIER90: A tool for obtaining maximally-localised Wannier functions, Comput. Phys. Commun. **178**, 685 (2008).

[46] A. A. Mostofi, J. R. Yates, G. Pizzi, Y.-S. Lee, I. Souza, D. Vanderbilt, and N. Marzari, An updated version of WANNIER90: A tool for obtaining maximally-localised Wannier functions, Comput. Phys. Commun. **185**, 2309 (2014).

[47] A. Damle, L. Lin, and L. Ying, SCDM-K: Localized orbitals for solids via selected columns of the density matrix, J. Comput. Phys. **334**, 1 (2017).

[48] M. G. Lopez, D. Vanderbilt, T. Thonhauser, and I. Souza, Wannier-based calculation of the orbital magnetization in crystals, Phys. Rev. B **85**, 014435 (2012).

[49] P. Giannozzi, S. Baroni, N. Bonini, M. Calandra, R. Car, C. Cavazzoni, D. Ceresoli, G. L. Chiarotti, M. Cococcioni, I. Dabo *et al.*, QUANTUM ESPRESSO: A modular and open-source software project for quantum simulations of materials, J. Phys.: Condens. Matter **21**, 395502 (2009).

[50] P. Giannozzi, O. Andreussi, T. Brumme, O. Bunau, M. B. Nardelli, M. Calandra, R. Car, C. Cavazzoni, D. Ceresoli, M. Cococcioni *et al.*, Advanced capabilities for materials modelling with QUANTUM ESPRESSO, J. Phys.: Condens. Matter **29**, 465901 (2017).

[51] D. R. Hamann, Optimized norm-conserving Vanderbilt pseudopotentials, Phys. Rev. B **88**, 085117 (2013).

[52] M. Schlipf and F. Gygi, Optimization algorithm for the generation of ONCV pseudopotentials, Comput. Phys. Commun. **196**, 36 (2015).

[53] P. Scherpelz, M. Govoni, I. Hamada, and G. Galli, Implementation and validation of fully relativistic GW calculations: Spin-orbit coupling in molecules, nanocrystals, and solids, J. Chem. Theory Comput. **12**, 3523 (2016).

[54] F. Giustino, Electron-phonon interactions from first principles, Rev. Mod. Phys. **89**, 015003 (2017).

[55] M. Bernardi, First-principles dynamics of electrons and phonons*, Eur. Phys. J. B **89**, 239 (2016).

[56] N. Marzari and D. Vanderbilt, Maximally localized generalized Wannier functions for composite energy Bands, Phys. Rev. B **56**, 12847 (1997).

[57] I. Souza, N. Marzari, and D. Vanderbilt, Maximally localized Wannier functions for entangled energy bands, Phys. Rev. B **65**, 035109 (2001).

[58] S. Poncé, E. R. Margine, C. Verdi, and F. Giustino, EPW: Electron-phonon coupling, transport and superconducting properties using maximally localized Wannier functions, Comput. Phys. Commun. **209**, 116 (2016).

[59] A. Togo and I. Tanaka, First principles phonon calculations in materials science, Scr. Mater. **108**, 1 (2015).

[60] A. Togo, L. Chaput, and I. Tanaka, Distributions of phonon lifetimes in Brillouin zones, Phys. Rev. B **91**, 094306 (2015).

[61] M.-Q. Le, H.-T. Nguyen, and T.-L. Bui, Fracture of 28 buckled two-dimensional hexagonal sheets, Mech. Adv. Mater. Struct. **29**, 4993 (2021).

[62] J. Shi, Y. Gao, X.-L. Wang, and S.-N. Yun, Electronic, elastic and piezoelectric properties of two-dimensional group-IV buckled monolayers, Chinese Phys. Lett. **34**, 087701 (2017).

[63] See Supplemental Material at http://link.aps.org/supplemental/10.1103/PhysRevB.107.035429 for the electronic band structure of SnX (X = Si, Ge) monolayers calculated using the G_0W_0 method, the band gap of SnSi as a function of different kinds of strains within the experimentally feasible range of $\pm 3\%$, the variation of the band gap of the SnGe monolayer with the application of biaxial strain ranging from -10 to $+10\%$ and evolution of the band structure, the band gap variation of the SnGe monolayer with the application of a vertical electric field, and a zoomed image of acoustic phonon spectra of SnSi and SnGe near the Γ point.

[64] X. Tang and L. Kou, 2D Janus transition metal dichalcogenides: Properties and applications, Phys. Status Solidi B **259**, 2100562 (2022).

[65] S.-B. Yu, M. Zhou, D. Zhang, and K. Chang, Spin Hall effect in the monolayer Janus compound MoSSe enhanced by Rashba spin-orbit coupling, Phys. Rev. B **104**, 075435 (2021).

[66] Q. Wei, D. Chen, Y. Cai, L. Shen, J. Xu, J. Yuan, Y. Chen, and X. Yan, Generation and enhancement of valley polarization in monolayer chromium dichalcogenides, J. Supercond. Nov. Magn. **35**, 787 (2022).

[67] Y. Lee, A. Knothe, H. Overweg, M. Eich, C. Gold, A. Kurzmann, V. Klasovika, T. Taniguchi, K. Wantanabe, V. Fal'ko *et al.*, Tunable Valley Splitting due to Topological Orbital Magnetic Moment in Bilayer Graphene Quantum Point Contacts, Phys. Rev. Lett. **124**, 126802 (2020).

[68] T. J. Lyon, J. Sichau, A. Dorn, A. Centeno, A. Pesquera, A. Zurutuza, and R. H. Blick, Probing Electron Spin Resonance in Monolayer Graphene, Phys. Rev. Lett. **119**, 066802 (2017).

[69] R. G. Mani, J. Hankinson, C. Berger, and W. A. de Heer, Observation of resistively detected hole spin resonance and zero-field pseudo-spin splitting in epitaxial graphene, Nat. Commun. **3**, 996 (2012).

[70] A. Kareekunnan, M. Muruganathan, and H. Mizuta, Manipulating Berry curvature in HBN/bilayer graphene commensurate heterostructures, Phys. Rev. B **101**, 195406 (2020).

[71] D. Xiao, M.-C. Chang, and Q. Niu, Berry phase effects on electronic properties, Rev. Mod. Phys. **82**, 1959 (2010).

[72] D. Ceresoli, T. Thonhauser, D. Vanderbilt, and R. Resta, Orbital magnetization in crystalline solids: Multi-band insulators, Chern insulators, and metals, Phys. Rev. B **74**, 024408 (2006).

[73] A. Knothe and V. Fal'ko, Influence of minivalleys and Berry curvature on electrostatically induced quantum wires in gapped bilayer graphene, Phys. Rev. B **98**, 155435 (2018).

[74] M.-C. Chang and Q. Niu, Berry Phase, Hyperorbits, and the Hofstadter Spectrum, Phys. Rev. Lett. **75**, 1348 (1995).

[75] D. J. Thouless, M. Kohmoto, M. P. Nightingale, and M. den Nijs, Quantized Hall Conductance in a Two-Dimensional Periodic Potential, Phys. Rev. Lett. **49**, 405 (1982).

[76] M. Gradhand, D. V. Fedorov, F. Pientka, P. Zahn, I. Mertig, and B. L. Györffy, First-principle calculations of the Berry curvature of Bloch states for charge and spin transport of electrons, J. Phys.: Condens. Matter **24**, 213202 (2012).

[77] H.-J. Kim, C. Li, J. Feng, J.-H. Cho, and Z. Zhang, Competing magnetic orderings and tunable topological states in two-dimensional hexagonal organometallic lattices, Phys. Rev. B **93**, 041404(R) (2016).

[78] X. Xu, W. Yao, D. Xiao, and T. F. Heinz, Spin and pseudospins in layered transition metal dichalcogenides, Nature Phys. **10**, 343 (2014).

[79] W. Du, R. Peng, Z. He, Y. Dai, B. Huang, and Y. Ma, Anomalous valley Hall effect in antiferromagnetic monolayers, npj 2D Mater. Appl. **6**, 11 (2022).

[80] E. Scalise, M. Houssa, G. Pourtois, V. Afanas'ev, and A. Stesmans, Strain-induced semiconductor to metal transition in the two-dimensional honeycomb structure of MoS_2, Nano Res. **5**, 43 (2012).

[81] E. Blundo, M. Felici, T. Yildirim, G. Pettinari, D. Tedeschi, A. Miriametro, B. Liu, W. Ma, Y. Lu, and A. Polimeni, Evidence of the direct-to-indirect band gap transition in strained two-dimensional WS_2, MoS_2, and WSe_2, Phys. Rev. Res. **2**, 012024(R) (2020).

[82] J. D. Leger, M. R. Friedfeld, R. A. Beck, J. D. Gaynor, A. Petrone, X. Li, B. M. Cossairt, and M. Khalil, Carboxylate anchors act as exciton reporters in 1.3 nm indium phosphide nanoclusters, J. Phys. Chem. Lett. **10**, 1833 (2019).

[83] X. Yang, B. Sa, H. Zhan, and Z. Sun, Electric field-modulated data storage in bilayer InSe, J. Mater. Chem. C **5**, 12228 (2017).

[84] H. Zhang, L. Kou, Y. Jiao, A. Du, Y. Tang, and Y. Ni, Strain engineering of selective chemical adsorption on monolayer black phosphorous, Appl. Surf. Sci. **503**, 144033 (2020).

[85] F. A. Rasmussen and K. S. Thygesen, Computational 2D materials database: Electronic structure of transition-metal dichalcogenides and oxides, J. Phys. Chem. C **119**, 13169 (2015).

[86] S. B. Desai, G. Seol, J. S. Kang, H. Fang, C. Battaglia, R. Kapadia, J. W. Ager, J. Guo, and A. Javey, Strain-induced indirect to direct bandgap transition in multilayer WSe_2, Nano Lett. **14**, 4592 (2014).

[87] V. Wang, N. Xu, J. C. Liu, G. Tang, and W.-T. Geng, VASPKIT: A user-friendly interface facilitating high-throughput computing and analysis using VASP code, Comput. Phys. Commun. **267**, 108033 (2021).

[88] M. K. Mohanta, F. Is, A. Kishore, and A. De Sarkar, Spin-current modulation in hexagonal buckled ZnTe and CdTe monolayers for self-powered flexible-piezo-spintronic devices, ACS Appl. Mater. Interfaces **13**, 40872 (2021).

[89] M. K. Mohanta, A. Arora, and A. D. Sarkar, Conflux of tunable Rashba effect and piezoelectricity in flexible magnesium

monochalcogenide monolayers for next-generation spintronic devices, Nanoscale **13**, 8210 (2021).

[90] K. N. Kudin, G. E. Scuseria, and B. I. Yakobson, C_2F, BN, and C nanoshell elasticity from *ab initio* computations, Phys. Rev. B **64**, 235406 (2001).

[91] R. C. Cooper, C. Lee, C. A. Marianetti, X. Wei, J. Hone, and J. W. Kysar, Nonlinear elastic behavior of two-dimensional molybdenum disulfide, Phys. Rev. B **87**, 035423 (2013).

[92] T. Lorenz, D. Teich, J.-O. Joswig, and G. Seifert, Theoretical study of the mechanical behavior of individual $TiS2$ and MoS_2 nanotubes, J. Phys. Chem. C **116**, 11714 (2012).

[93] M. K. Mohanta, A. R. Dimple, N. Jena, R. Ahammed, and A. De Sarkar, Ultra-low thermal conductivity and super-slow hot-carrier thermalization induced by a huge phononic gap in multifunctional nanoscale boron pnictides, Physica E **124**, 114222 (2020).

[94] J. Bardeen and W. Shockley, Deformation potentials and mobilities in non-polar crystals, Phys. Rev. **80**, 72 (1950).

[95] X. Chen, J. Lin, Q. Lin, R. Li, G. Xia, W. Zou, and X. Yu, Two-dimensional CP_2 and $Li_x CP_2$ ($x = 1$ and 2) monolayer with high-mobility transport anisotropy and extraordinary optical properties, Phys. Rev. B **106**, 075402 (2022).

[96] G. Zhang, K. Lu, Y. Wang, H. Wang, and Q. Chen, Mechanical and electronic properties of α-M_2X_3 ($M =$ Ga, In; $X =$ S, Se) monolayers, Phys. Rev. B **105**, 235303 (2022).

[97] K. Kaasbjerg, K. S. Thygesen, and K. W. Jacobsen, Phonon-limited mobility in n-type single-layer MoS_2 from first principles, Phys. Rev. B **85**, 115317 (2012).

[98] L. Cheng and Y. Liu, What limits the intrinsic mobility of electrons and holes in two dimensional metal dichalcogenides? J. Am. Chem. Soc. **140**, 17895 (2018).

[99] S. Poncé, W. Li, S. Reichardt, and F. Giustino, First-principles calculations of charge carrier mobility and conductivity in bulk semiconductors and two-dimensional materials, Rep. Prog. Phys. **83**, 036501 (2020).

[100] S. Mu, A. J. E. Rowberg, J. Leveillee, F. Giustino, and C. G. Van de Walle, First-principles study of electron transport in ScN, Phys. Rev. B **104**, 075118 (2021).

[101] S. Poncé, E. R. Margine, and F. Giustino, Towards predictive many-body calculations of phonon-limited carrier mobilities in semiconductors, Phys. Rev. B **97**, 121201(R) (2018).

[102] S. Takagi, A. Toriumi, M. Iwase, and H. Tango, On the universality of inversion layer mobility in Si MOSFET's: Part I—Effects of substrate impurity concentration, IEEE Trans. Electron Devices **41**, 2357 (1994).

[103] S. Takagi, J. L. Hoyt, J. J. Welser, and J. F. Gibbons, Comparative study of phonon-limited mobility of two-dimensional electrons in strained and unstrained Si metal–oxide–semiconductor field-effect transistors, J. Appl. Phys. **80**, 1567 (1996).

[104] H. Lang, S. Zhang, and Z. Liu, Mobility anisotropy of two-dimensional semiconductors, Phys. Rev. B **94**, 235306 (2016).

[105] M. Xie, S. Zhang, B. Cai, Z. Zhu, Y. Zou, and H. Zeng, Two-dimensional BX ($X =$ P, As, Sb) semiconductors with mobilities approaching graphene, Nanoscale **8**, 13407 (2016).

[106] S. H. Mir, V. K. Yadav, and J. K. Singh, Recent advances in the carrier mobility of two-dimensional materials: A theoretical perspective, ACS Omega **5**, 14203 (2020).

[107] A. Rawat, N. Jena, Dimple, and A. D. Sarkar, A comprehensive study on carrier mobility and artificial photosynthetic properties in group VI B transition metal dichalcogenide monolayers, J. Mater. Chem. A **6**, 8693 (2018).

[108] A. J. H. McGaughey, E. S. Landry, D. P. Sellan, and C. H. Amon, Size-dependent model for thin film and nanowire thermal conductivity, Appl. Phys. Lett. **99**, 131904 (2011).

[109] M. K. Mohanta, A. Rawat, N. Jena, R. Ahammed, and A. D. Sarkar, Superhigh flexibility and out-of-plane piezoelectricity together with strong anharmonic phonon scattering induced extremely low lattice thermal conductivity in hexagonal buckled CdX ($X =$ S, Se) monolayers, J. Phys.: Condens. Matter **32**, 355301 (2020).

[110] B. Peng, H. Zhang, H. Shao, Y. Xu, G. Ni, R. Zhang, and H. Zhu, Phonon transport properties of two-dimensional group-IV materials from *ab initio* calculations, Phys. Rev. B **94**, 245420 (2016).

[111] A. Jain and A. J. H. McGaughey, Strongly anisotropic in-plane thermal transport in single-layer black phosphorene, Sci. Rep. **5**, 8501 (2015).

[112] X. Li, J. T. Mullen, Z. Jin, K. M. Borysenko, M. Buongiorno Nardelli, and K. W. Kim, Intrinsic electrical transport properties of monolayer silicene and MoS_2 from first principles, Phys. Rev. B **87**, 115418 (2013).

[113] B. Peng, H. Zhang, H. Shao, Y. Xu, X. Zhang, and H. Zhu, Low lattice thermal conductivity of stanene, Sci. Rep. **6**, 20225 (2016).

[114] P.-F. Liu, T. Bo, J. Xu, W. Yin, J. Zhang, F. Wang, O. Eriksson, and B.-T. Wang, First-principles calculations of the ultralow thermal conductivity in two-dimensional group-IV selenides, Phys. Rev. B **98**, 235426 (2018).

[115] G. A. Slack, Nonmetallic crystals with high thermal conductivity, J. Phys. Chem. Solids **34**, 321 (1973).

[116] A. Shafique, A. Samad, and Y.-H. Shin, Ultra low lattice thermal conductivity and high carrier mobility of monolayer SnS_2 and $SnSe_2$: A first principles study, Phys. Chem. Chem. Phys. **19**, 20677 (2017).

[117] S.-D. Guo and J.-T. Liu, Lower lattice thermal conductivity in SbAs than As or Sb monolayers: A first-principles study, Phys. Chem. Chem. Phys. **19**, 31982 (2017).

[118] A. Shafique and Y.-H. Shin, Thermoelectric and phonon transport properties of two-dimensional IV–VI compounds, Sci. Rep. **7**, 506 (2017).

[119] B. Peng, H. Zhang, H. Shao, Y. Xu, R. Zhang, H. Lu, D. W. Zhang, and H. Zhu, First-principles prediction of ultralow lattice thermal conductivity of dumbbell silicene: A comparison with low-buckled silicene, ACS Appl. Mater. Interfaces **8**, 20977 (2016).